Deepwater Formation in the North Pacific During the Last Glacial Termination

Y. Okazaki, *et al.*

Science **329**, 200 (2010);
DOI: 10.1126/science.1190612

mers (Eq. 4 and eqs. S7 and S9, respectively). For example, the fraction of the long arm with degree of polymerization X_L was determined as in (*33*)

$$P_L(X_L) = \frac{p^{X_L}\sum_{X_M=1}^{X_L} p^{X_M}\sum_{X_S=1}^{X_M} p^{X_S}}{\sum_{X_L=1}^{\infty} p^{X_L}\sum_{X_M=1}^{X_L} p^{X_M}\sum_{X_S=1}^{X_M} p^{X_S}} = (1-p^3)(p^{X_L-1}-p^{2X_L-1}-p^{2X_L}+p^{3X_L}) \quad (4)$$

The experimental and theoretical distributions of the arm length in star molecules were in good agreement (Fig. 3B).

In the branching points, we observed three types of mutual orientation of the NRs (Fig. 3C). We labeled the junctions as $J_{3\|\text{-}\|}$, $J_{3\perp\text{-}\perp}$, and $J_{3\|\text{-}\perp}$ where the number 3 in the subscripts denotes the number of NRs in the junction, and the symbols ||-||, ⊥-⊥, and ||-⊥ reflect two parallel, two perpendicular, and one parallel/one perpendicular NR alignments, respectively. The histogram of the fractions of each type of junction in the chains showed a lower fraction of $J_{3\|\text{-}\|}$ junctions in comparison with $J_{3\perp\text{-}\perp}$ and $J_{3\|\text{-}\perp}$ junctions (Fig. 3D), due to the steric constraints in attaching the second NR in the parallel orientation to the reacted arrowhead.

The polymerization model was applicable to the self-assembly of arrowhead and cylindrical gold NRs (*28*), with a length in the range from 30 to 50 nm, which were end-tethered with PS molecules with a molecular weight ranging from 5000 to 20000 g/mol. We anticipate that the approach can be applied to the organization of other types of NPs, as long as their self-assembly follows a reaction-limited process.

This work bridges the gap between polymerization reactions taking place at a molecular level and NP self-assembly occurring at the length scale two orders of magnitude larger. It shows that the theory of step-growth polymerization is valid for the assembly of NPs linked by physical bonds. The polymerization approach enables pre-programming the dimensions of 1D nanostructures by assembling NP chains with a predetermined length. It can facilitate the design of new, complex nanostructures by mimicking a large library of polymers produced by step-growth polymerization, e.g., hyperbranched (dendritic) polymers, polymer networks, and copolymerization of different NPs (e.g., metal and semiconductor NPs) with a high degree of control over the structure of alternating, block and graft-copolymers. Owing to the progress in NP synthesis, the self-assembly of NPs with asymmetric functional groups can be explored and modeled using the theory developed for polymerization of more complex monomers. On the other hand, the capability to visualize the polymerization process by imaging emerging nanostructures provides the unique ability to test theoretical models developed for step-growth polymerization.

References and Notes

1. Z. Nie, A. Petukhova, E. Kumacheva, *Nat. Nanotechnol.* **5**, 15 (2010).
2. S. C. Glotzer *et al.*, *Curr. Opin. Colloid Interface Sci.* **10**, 287 (2005).
3. S. C. Glotzer, M. J. Solomon, *Nat. Mater.* **6**, 557 (2007).
4. G. A. DeVries *et al.*, *Science* **315**, 358 (2007).
5. W. U. Huynh, J. J. Dittmer, A. P. Alivisatos, *Science* **295**, 2425 (2002).
6. M. Rycenga, J. M. McLellan, Y. Xia, *Adv. Mater.* **20**, 2416 (2008).
7. Z. Tang, N. A. Kotov, M. Giersig, *Science* **297**, 237 (2002).
8. A. Courty, A. Mermet, P. A. Albouy, E. Duval, M. P. Pileni, *Nat. Mater.* **4**, 395 (2005).
9. D. Zerrouki, J. Baudry, D. Pine, P. Chaikin, J. Bibette, *Nature* **455**, 380 (2008).
10. Z. Nie *et al.*, *Nat. Mater.* **6**, 609 (2007).
11. S. A. Maier *et al.*, *Nat. Mater.* **2**, 229 (2003).
12. S. A. Maier *et al.*, *Adv. Mater.* **13**, 1501 (2001).
13. W. Nomura, M. Ohtsu, T. Yatsui, *Appl. Phys. Lett.* **86**, 181108 (2005).
14. C.-J. Wang, L. Huang, B. A. Parviz, L. Y. Lin, *Nano Lett.* **6**, 2549 (2006).
15. T. Yatsui *et al.*, *Appl. Phys. Lett.* **96**, 133106 (2010).
16. J. N. Anker *et al.*, *Nat. Mater.* **7**, 442 (2008).
17. G. Kawamura, Y. Yang, M. Nogami, *Appl. Phys. Lett.* **90**, 261908 (2007).
18. Z. Nie, D. Fava, M. Rubinstein, E. Kumacheva, *J. Am. Chem. Soc.* **130**, 3683 (2008).
19. M. E. Leunissen *et al.*, *Nat. Mater.* **8**, 590 (2009).
20. K. K. Caswell, J. N. Wilson, U. H. F. Bunz, C. J. Murphy, *J. Am. Chem. Soc.* **125**, 13914 (2003).
21. K. D. Hermanson, S. O. Lumsdon, J. P. Williams, E. W. Kaler, O. D. Velev, *Science* **294**, 1082 (2001).
22. C. Ribeiro, E. J. H. Lee, E. Longo, E. R. Leite, *ChemPhysChem* **7**, 664 (2006).
23. S. Shanbhag, Z. Tang, N. A. Kotov, *ACS Nano* **1**, 126 (2007).
24. P. J. Flory, *Principles of Polymer Chemistry* (Cornell Univ. Press, New York, 1953).
25. G. Odian, *Principles of Polymerization* (Wiley, New York, ed. 4, 2004).
26. S. Kuchanov, H. Slot, A. Stroeks, *Prog. Polym. Sci.* **29**, 563 (2004).
27. Materials and methods are available as supporting material on *Science* Online.
28. B. Nikoobakht, M. A. El-Sayed, *Chem. Mater.* **15**, 1957 (2003).
29. Y. Xiang *et al.*, *J. Phys. Chem. C* **112**, 3203 (2008).
30. Evidence that chain formation occurred in solution, as opposed to being caused by solvent evaporation, was obtained in light-scattering and UV-visible spectroscopy experiments, as well as in the control experiments conducted at different solvent evaporation rates and on different substrates.
31. C. J. Orendorff, C. J. Murphy, *J. Phys. Chem. B* **110**, 3990 (2006).
32. In the control experiments, the time of bond formation was markedly reduced for the self-assembly of cylindrical Au nanorods end-terminated with thiolated PS, which did not require specific orientation of the NR during bond formation.
33. M. Rubinstein, R. H. Colby, *Polymer Physics* (Oxford Univ. Press, Oxford, 2003).

34. We thank the National Science and Engineering Research Council of Canada (under Discovery program and Canada Research Chair program) for financial support. M.R. acknowledges financial support from the NSF under grants CHE-0911588, DMR-0907515, and CBET-0609087 and the NIH under grant 1-R01-HL077546-03A2. The authors are grateful to Y. Chen and G. Wu for their contribution in image analysis.

Supporting Online Material

www.sciencemag.org/cgi/content/full/329/5988/197/DC1
Materials and Methods
SOM Text
Figs. S1 to S3
Tables S1
References

11 March 2010; accepted 2 June 2010
10.1126/science.1189457

Deepwater Formation in the North Pacific During the Last Glacial Termination

Y. Okazaki,[1] A. Timmermann,[2]* L. Menviel,[2] N. Harada,[1] A. Abe-Ouchi,[1,3] M. O. Chikamoto,[1] A. Mouchet,[4] H. Asahi[3]

Between ~17,500 and 15,000 years ago, the Atlantic meridional overturning circulation weakened substantially in response to meltwater discharges from disintegrating Northern Hemispheric glacial ice sheets. The global effects of this reorganization of poleward heat flow in the North Atlantic extended to Antarctica and the North Pacific. Here we present evidence from North Pacific paleo surface proxy data, a compilation of marine radiocarbon age ventilation records, and global climate model simulations to suggest that during the early stages of the Last Glacial Termination, deep water extending to a depth of ~2500 to 3000 meters was formed in the North Pacific. A switch of deepwater formation between the North Atlantic and the North Pacific played a key role in regulating poleward oceanic heat transport during the Last Glacial Termination.

Massive meltwater discharges during the Last Glacial Termination [~19 to 10 thousand years ago (ka)], such as Heinrich event 1 (H1: ~17.5 to 15 ka) and the Younger Dryas event (YD: ~13 to 11.5 ka), reduced North Atlantic surface density conditions and interrupted the steady flow of the Atlantic meridional overturning circulation (AMOC) (*1*). Through atmospheric and oceanic teleconnections, climate conditions changed substantially in the North Pacific, as documented by numerical climate modeling studies (*2*–*4*) and paleo-proxy data (*5*, *6*).

Recent studies (*7*–*11*) using data obtained from single-sediment cores in the North Pacific reported local evidence for major reorganizations of the North Pacific Ocean circulation during H1, the Bølling-Allerød (BA: ~14.5 to 13 ka) warm period, and the YD. The interpretation of radiocarbon data in these cores reveals that during H1,

very old water masses seeped into intermediate layers of the eastern tropical Pacific, whereas the western North Pacific sites near Japan show relatively young radiocarbon ventilation ages at intermediate depths (1000 to 2000 m). Understanding the mechanisms by which old carbon-rich water from the deep North Pacific was vented to the surface and replaced by younger water masses may also hold important clues toward resolving the puzzle of the carbon sources that caused the rise of atmospheric CO_2 during the last deglaciation.

The goal of this study is to provide a more comprehensive view of what triggered ventilation changes in the North Pacific during the early deglaciation and to reconstruct spatial patterns and pathways of intermediate-deepwater circulation. For these purposes, we compiled a comprehensive data set of published radiocarbon sediment core data from the North Pacific with temporal coverage large enough to resolve the H1/BA transition (*12*). Together with a climate model simulation that mimics H1, we used these data to determine the effects of AMOC changes on the large-scale conveyor-belt circulation, with an emphasis on the North Pacific.

To better understand the driving mechanisms of North Pacific circulation changes, we provide an overview of North Pacific climate conditions during the Last Glacial Termination (Fig. 1). During H1, a time of weak AMOC (Fig. 1A) (*1*), the eastern subarctic Pacific was warm and relatively saline, as documented by dinocyst assemblages in core PAR87A-10 [54.36°N, 148.47°W, 3664-m water depth (*13*)] (Fig. 1, B and C). Planktonic foraminiferal Mg/Ca and $\delta^{18}O$ analyses in core GH02-1030 [42.23°N, 144.21°E, 1212-m water depth (*14*)] in the western North Pacific reveal the presence of cold and saline surface waters during the early deglaciation (Fig. 1, D and E).

As documented by these analyses, salinity dropped in the eastern and western North Pacific after ~16 thousand years, attaining minimum values during BA. By accounting for dating uncertainties among the different cores, we found that the drop of surface salinity during the H1/BA transition coincided with an increase in near-bottom phosphate contents inferred from benthic foraminiferal $\delta^{13}C$ values in cores MR01K03-PC4 from the western North Pacific [41.12°N, 142.40°E, 1366-m water depth (*15*)] and BOW9A from the Bering Sea (54.04°N, 178.68°E, 2391-m water depth) (Fig. 1F). This change in the western North Pacific indicates a transition from nutrient-depleted and well-ventilated intermediate-deep waters during H1 to nutrient-enriched less-ventilated waters during BA.

The reduced abundance of dysaerobic benthic foraminiferal taxa in the Bering Sea core BOW9A during H1 compared with that in the BA period (*16*) is also consistent with the notion of enhanced deepwater ventilation extending to a depth of ~2500 m (Fig. 1G). Oxygen-rich intermediate-deep waters during H1 were also reconstructed

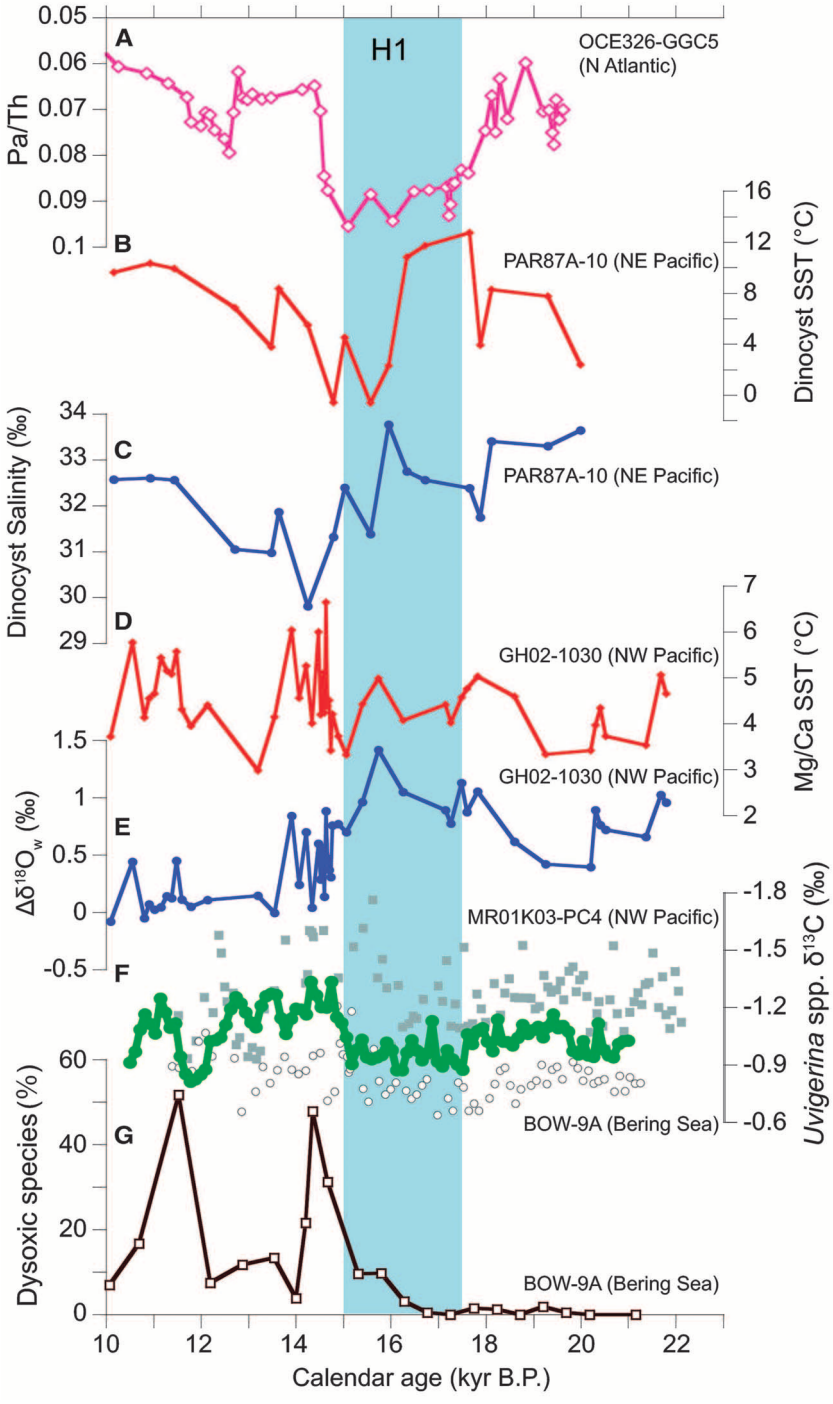

Fig. 1. Sediment proxy records in the North Pacific from 23 to 10 ka on their re-established time scales (table S2) with (**A**) Pa/Th ratio as a proxy for the AMOC strength in the North Atlantic (*1*); sea-surface temperature and salinity changes in (**B** and **C**) the eastern North Pacific based on dinocyst assemblages (*13*) and in (**D** and **E**) the western North Pacific based on planktonic foraminiferal Mg/Ca and $\delta^{18}O$ (*14*); (**F**) raw benthic foraminiferal $\delta^{13}C$ data in the western North Pacific (*15*) (1366 m, gray squares), the Bering Sea (2391 m, open circles), and spline-interpolated and averaged benthic $\delta^{13}C$ values (green circles); and (**G**) percentage of dysaerobic benthic foraminifera species in the Bering Sea (2391 m) (*16*).

[1]Japan Agency for Marine-Earth Science and Technology, 2-15 Natsushima-cho, Yokosuka 237-0061, Japan. [2]International Pacific Research Center, School of Ocean and Earth Science and Technology, University of Hawaii, 2525 Correa Road, Honolulu, HI 96822, USA. [3]Atmosphere and Ocean Research Institute, University of Tokyo, 5-1-5 Kashiwanoha, Kashiwa 277-8568, Japan. [4]Université de Liège, Laboratoire de physique atmosphérique et planétaire, Allée du Six-Août 17, BAT B5C, 4000 Liège, Belgium.

*To whom correspondence should be addressed. E-mail: axel@hawaii.edu

from benthic foraminiferal assemblages (*17*) and redox-sensitive metals (*18*) in records from the western North Pacific. Because the millennial-scale variations in oxygen concentrations found in these cores are out of phase with those obtained from deeper sites in the North Pacific (ODP882 at 3200 m, and ODP887 at 3600 m) (*9*), we estimate the maximum vertical extent of North Pacific intermediate to deep water spreading during H1 to be ~3000 m. When this value is compared with present-day values of about 800 m (*19*), it becomes evident that such changes would have required a major reorganization of the entire North Pacific ocean circulation.

To develop a better understanding of the nature of ocean circulation changes during the deglaciation, we compiled published radiocarbon data from 29 intermediate-deepwater cores in the North Pacific (table S1). ^{14}C ages were converted to calendar ages on planktonic foraminifera samples from these cores using the Calib 6.0 routine with the Marine09 calibration data set (*20*). Ventilation ages estimated from ^{14}C age differences between coexisting benthic and planktonic foraminifera shells (BF–PF age), projection ages (*21*) (table S3), and reconstructed bottom water $\Delta^{14}C$ activities (*9*) (table S4) were then calculated for all cores.

The compilation of western North Pacific radiocarbon ages (Fig. 2, for depth range 900 to 2800 m) reveals notable changes in deepwater ventilation during the last deglaciation. By averaging radiocarbon age estimates derived from the projection method and the BF–PF method, we obtained ventilation age estimates for the Last Glacial Maximum (LGM: ~23 to 19 ka), H1 (~17.5 to 15 ka), and BA (14.5 to 13 ka) periods of ~1500 years, ~950 years, and ~1550 years, respectively. The ~600-year drop in ventilation age between the LGM and H1 is significantly larger than the typical one-sided uncertainties in the projection method during this time (385 years), which supports the notion of a major reorganization of North Pacific intermediate-deepwater flow during H1.

No coherent averaged projection and BF–PF age ventilation changes were observed between the LGM (~1540 years), H1 (~1450 years), and BA (~1600 years) in the eastern North Pacific (900 to 2800 m) (table S5 and fig. S6). These findings for the western and eastern North Pacific are consistent with reconstructed bottom water $\Delta^{14}C$ activities (table S5). The presence of a well-ventilated water mass above 2000 m, the so-called glacial North Pacific intermediate water (GNPIW), has been suggested previously for LGM conditions (*22*, *23*), with the Bering Sea being the source of this water mass (*24*). Our reconstructed ventilation changes during H1 show a much more pronounced reorganization of deep western North Pacific flow.

To explore how this reorganization of deep North Pacific flow in response to changes of the AMOC came about, freshwater perturbation experiments were conducted with the Earth system model of intermediate complexity LOVECLIM (version 1.1) (*25*, *26*) under both preindustrial and LGM background conditions. These experiments enabled us to compare simulated changes in radiocarbon with those reconstructed by the sediment core compilation (table S3). The freshwater perturbation experiments simulate the climate response to an idealized glacial meltwater pulse that mimics H1. By linearly increasing the freshwater forcing to 2 Sv in the northern North Atlantic for 100 years, the water becomes less dense, leading to a reduction of deep convection in the North Atlantic and a subsequent collapse of the AMOC. An associated reduction of poleward heat transport leads to large-scale cooling in the Northern Hemisphere, as in other climate models (*2*–*4*). Air-sea interactions in the North Atlantic and emanating atmospheric teleconnections are vital for cooling the western North Pacific (*4*). Furthermore, in response to the AMOC weakening and the associated North Atlantic cooling, the Atlantic-Pacific moisture transport weakens (*25*) and the Pacific Intertropical Convergence Zone shifts south, leading to a persistent reduction of precipitation and hence an overall increase of surface salinity in the North Pacific. Once the Pacific meridional overturning cell (PMOC) establishes, the anomalous poleward surface currents (fig. S3) transport more saline subtropical waters into the North Pacific, thereby providing a positive-salinity feedback. A closed Bering Strait facilitates the build-up of such North Pacific salinity anomalies (*27*). The resulting changes in surface density trigger deep oceanic convection in the subarctic Pacific. The three-dimensional adjustment to the resulting North Pacific density anomalies in the preindustrial and LGM LOVECLIM1.1 freshwater perturbation experiment leads to the establishment of a deep PMOC (Fig. 3B and fig. S2), which distributes young and oxygen-rich deep water throughout the entire western North Pacific down to ~2500 m (Fig. 3B), in accordance with reconstructions of oxygen conditions in BOW9A (Fig. 1G).

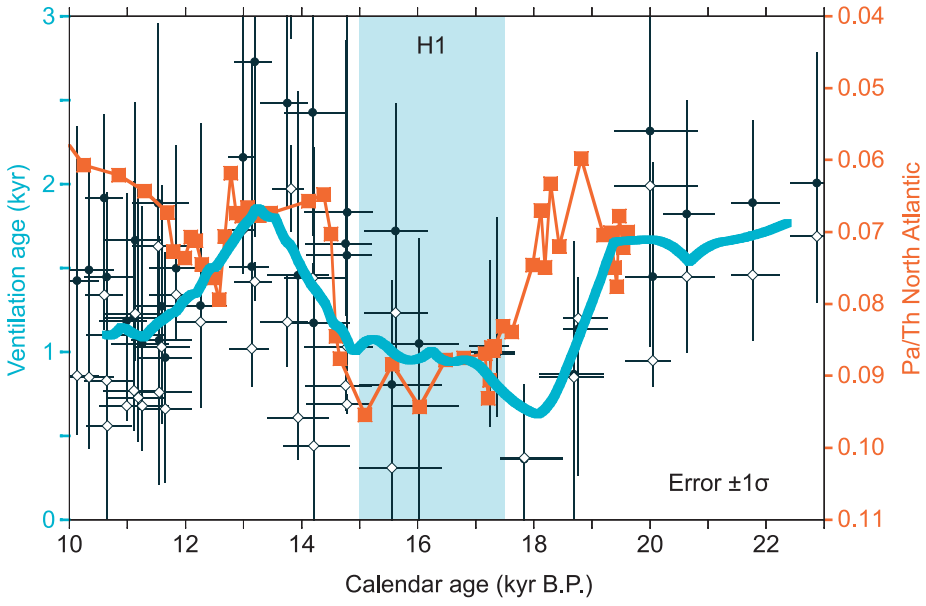

Fig. 2. Compilation of ventilation age changes based on published radiocarbon data in the western North Pacific (*8*, *14*, *30*–*32*). BF–PF ages (open diamonds), projection ages (gray circles), and smoothed spline interpolation of averaged BF–PF and projection ages (blue line). Uncertainty of calendar age and ventilation age is 1σ; Pa/Th ratio (orange squares) as a proxy for the AMOC strength in the North Atlantic (*1*).

Both model results (Fig. 3C) and paleo reconstructions (Fig. 1, B and D) suggest the existence of an east-west sea surface temperature gradient in the North Pacific during H1. The simulated cooling in the western North Pacific can be partly explained in terms of an intensification of the Aleutian Low (*4*) and cold-air advection. Simulated warming in the eastern North Pacific results from an enhanced poleward advection of heat, which is associated with the northeastward-flowing surface branch of the PMOC (Fig. 3C). Moreover, a very pronounced east-west gradient in intermediate-deepwater ventilation (Fig. 3D) is found, both in the paleoproxy reconstructions and the modeling experiments. The main simulated pathway of deepwater circulation is along the western margin of the North Pacific, in a deep western boundary current that is analogous to the one currently in the North Atlantic. The model results demonstrate that the western boundary flow is the principal factor in establishing the east-west gradient of intermediate-deep Pacific ventilation, which is also evident in the compilation of radiocarbon-based ventilation data (Fig. 3, A and D).

However, simulated radiocarbon age anomalies associated with the onset of the PMOC are too weak to explain the data from recent eastern Pacific intermediate-depth sediment cores (*10*, *11*) that reveal the presence of extremely old

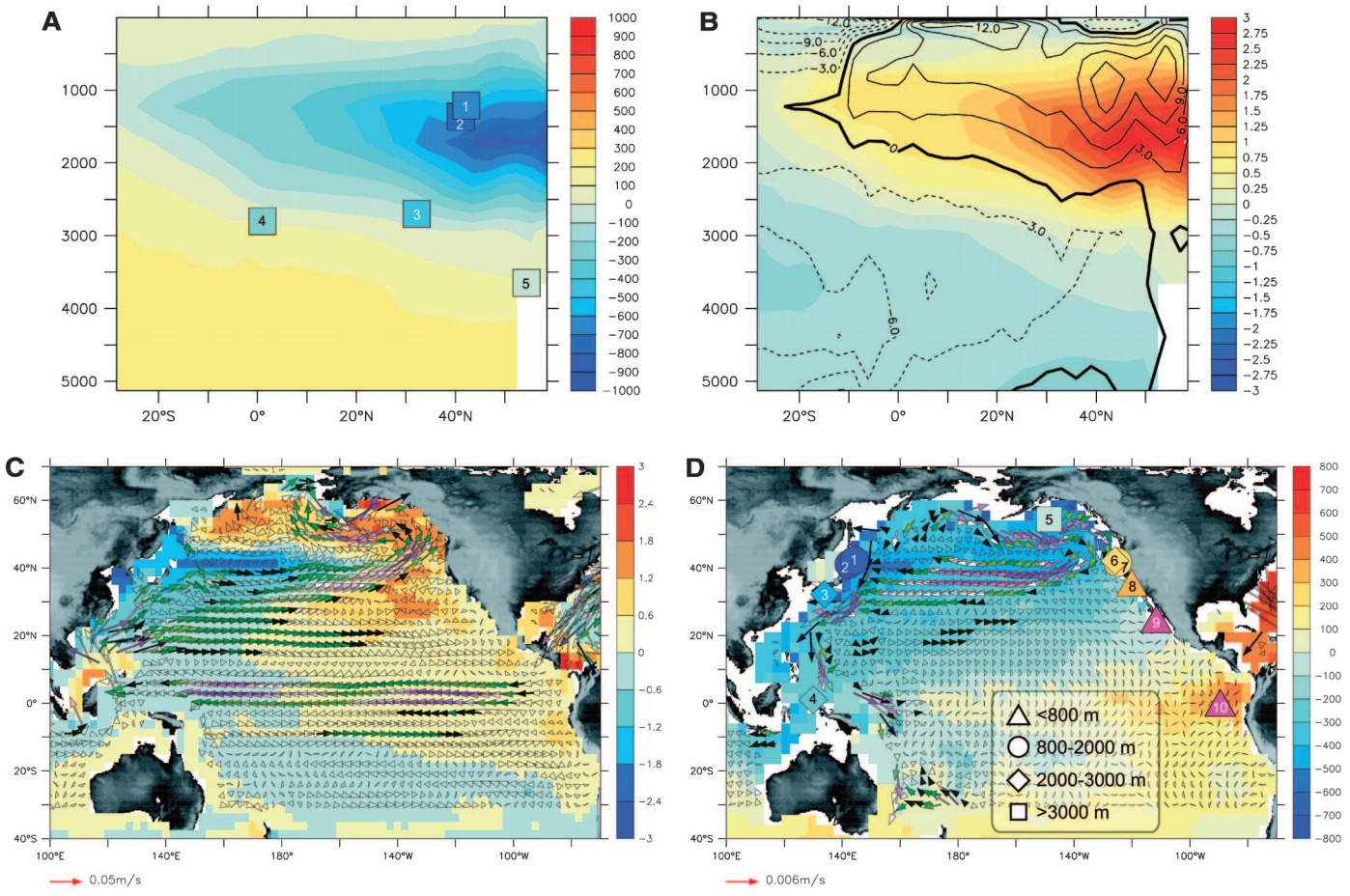

Fig. 3. (**A**) The shading indicates the sections of zonally averaged simulated radiocarbon age anomalies (in years) in the North Pacific between a collapsed AMOC state (years 400 to 500 of the freshwater experiment) and the control simulation using preindustrial background conditions. The squares indicate the reconstructed projection age anomaly (in years) (colored shading) of western North Pacific cores (*8*, *9*, *14*, *31*, *33*) (numbers of cores refer to table S1). (**B**) Shading indicates simulated zonally averaged Pacific oxygen anomalies (in ml oxygen per l of water) between a collapsed AMOC state (years 400 to 500 of the freshwater experiment) and the preindustrial control simulation. The contours indicate the simulated Pacific mean meridional stream function (10^6 m^3/s) (years 400 to 500 of the freshwater experiment). (**C**) Simulated upper ocean (0 to 65 m) temperature (shading) (°C) and velocity (vectors) (m/s) anomalies between collapsed AMOC state (years 400 to 500 of the freshwater perturbation experiment) and control simulation, using preindustrial background conditions. (**D**) Colored symbols indicate the projection age anomalies (in years) between H1 and the LGM (*8*–*11*, *14*, *31*, *33*–*35*) of radiocarbon data used in this analysis (numbers in symbols refer to table S1). The shading indicates simulated deep (1225 to 2963 m) minus near-surface (0 to 20 m) radiocarbon age anomalies (in years) between collapsed AMOC state (years 400 to 500 of the freshwater perturbation experiment) and control simulation. The arrows indicate the anomalous deep ocean currents averaged between 1225 and 2963 m.

intermediate water. To explain the very old eastern tropical Pacific intermediate waters during H1, a process unrelated to the onset of a PMOC has to be invoked (*11*).

The match between the simulated ventilation age anomalies in the western North Pacific and those reconstructed from a compilation of radiocarbon records (Fig. 3, A and D) makes a compelling case for the existence of a deep PMOC during H1 and an associated see-saw in deepwater formation between the North Atlantic and Pacific.

In our preindustrial and LGM freshwater perturbation experiments, the PMOC is maintained by the poleward advection of salinity from the subtropical regions (fig. S3) (*3*, *28*), a southward shifted Intertropical Convergence Zone, and reduced atmospheric export of fresh water from the Atlantic to the Pacific (*25*). As a result of the reorganization of the global conveyor belt circulation, the simulated Indonesian Throughflow weakens by 30 to 50% (*25*), which leads to a strengthening of the Kuroshio and the intrusion of North Pacific Intermediate Water into the tropical Pacific intermediate layers (*29*).

The shutdown of the AMOC in our model reduces the Atlantic heat transport at 40°N by ~0.6 PW (1 PW = 10^{15} W). At the same time, and in response to the establishment of a PMOC, poleward heat transport in the Pacific at 40°N increases by 0.4 PW. The PMOC hence played an important role in buffering the decrease in the poleward global oceanic heat transport caused by the shutdown of the AMOC. The evidence presented here demonstrates that the North Pacific was a very active region of thermohaline flow during the deglaciation and operated out of phase with the North Atlantic (Fig. 2). Viewing the North Pacific as participating in the ventilation of the global oceans could also help to explain the release of old carbon during the Last Glacial Termination.

References and Notes

1. J. F. McManus, R. Francois, J. M. Gherardi, L. D. Keigwin, S. Brown-Leger, *Nature* **428**, 834 (2004).
2. U. Mikolajewicz, T. J. Crowley, A. Schiller, R. Voss, *Nature* **387**, 384 (1997).
3. O. A. Saenko, A. Schmittner, A. J. Weaver, *J. Clim.* **17**, 2033 (2004).
4. Y. M. Okumura, C. Deser, A. Hu, A. Timmermann, S. P. Xie, *J. Clim.* **22**, 1424 (2009).
5. T. Kiefer, M. Kienast, *Quat. Sci. Rev.* **24**, 1063 (2005).
6. E. A. Boyle, L. Keigwin, *Nature* **330**, 35 (1987).
7. M. Sarnthein, P. M. Grootes, J. P. Kennett, M.-J. Nadeau, in *Ocean Circulation: Mechanisms and Impacts*, A. Schmittner, J. C. H. Chiang, S. R. Hemming, Eds. (American Geophysical Union, Washington, DC, 2007), pp. 175–197.
8. N. Ahagon, K. Ohkushi, M. Uchida, T. Mishima, *Geophys. Res. Lett.* **30**, 2097 (2003).
9. E. D. Galbraith *et al.*, *Nature* **449**, 890 (2007).

10. T. M. Marchitto, S. J. Lehman, J. D. Ortiz, J. Flückiger, A. van Geen, *Science* **316**, 1456 (2007).
11. L. Stott, J. Southon, A. Timmermann, A. Koutavas, *Paleoceanography* **24**, PA2223 (2009).
12. Materials and methods are available as supporting material on *Science* Online.
13. A. de Vernal, T. F. Pedersen, *Paleoceanography* **12**, 821 (1997).
14. T. Sagawa, K. Ikehara, *Geophys. Res. Lett.* **35**, L24702 (2008).
15. M. Hoshiba *et al.*, *Mar. Micropaleontol.* **61**, 196 (2006).
16. Y. Okazaki *et al.*, *Deep Sea Res. Part II Top. Stud. Oceanogr.* **52**, 2150 (2005).
17. A. Shibahara, K. Ohkushi, J. P. Kennett, K. Ikehara, *Paleoceanography* **22**, PA3213 (2007).
18. J. Crusius, T. F. Pedersen, S. Kienast, L. Keigwin, L. Labeyrie, *Geology* **32**, 633 (2004).
19. L. D. Talley, *J. Phys. Oceanogr.* **23**, 517 (1993).
20. P. J. Reimer *et al.*, *Radiocarbon* **51**, 1111 (2009).
21. J. F. Adkins, E. A. Boyle, *Paleoceanography* **12**, 337 (1997).
22. L. D. Keigwin, *Paleoceanography* **13**, 323 (1998).
23. K. Matsumoto, T. Oba, J. Lynch-Stieglitz, H. Yamamoto, *Quat. Sci. Rev.* **21**, 1693 (2002).
24. K. Horikawa, Y. Asahara, K. Yamamoto, Y. Okazaki, *Geology* **38**, 435 (2010).
25. U. Krebs, A. Timmermann, *J. Clim.* **20**, 4940 (2007).
26. L. Menviel, A. Timmermann, A. Mouchet, O. Timm, *Paleoceanography* **23**, PA1203 (2008).
27. A. Hu, G. A. Meehl, W. Han, *Geophys. Res. Lett.* **34**, L05704 (2007).
28. H. M. Stommel, *Tellus* **13**, 224 (1961).
29. J. P. McCreary Jr., P. Lu, *J. Phys. Oceanogr.* **31**, 932 (2001).
30. J. C. Duplessy *et al.*, *Radiocarbon* **31**, 493 (1989).
31. M. Murayama, A. Taira, H. Iwakura, E. Matsumoto, T. Nakamura, *Summaries of Researches Using AMS at Nagoya University* (Nagoya University Center for Chronological Research, Nagoya, Japan, vol. 3, 1992), pp. 114–121.
32. K. Minoshima *et al.*, *Mater. Atoms* **259**, 448 (2007).
33. W. Broecker, E. Clark, S. Barker, *Earth Planet. Sci. Lett.* **274**, 322 (2008).
34. A. C. Mix *et al.*, in *Mechanisms of Global Climate Change at Millennial Time Scales*, P. U. Clark, R. S. Webb, L. D. Keigwin, Eds. (American Geophysical Union, Washington, DC, 1999), pp. 127–148.
35. J. P. Kennett, B. L. Ingram, *Nature* **377**, 510 (1995).
36. This research was supported by NSF grant number ATM-0712690. Additional support was provided by the Japan Agency for Marine-Earth Science and Technology (JAMSTEC), by NASA through grant number NNX07AG53G, and by the National Oceanic and Atmospheric Administration through grant number NA09OAR4320075, all of which sponsor research at the International Pacific Research Center. A.M. acknowledges funding from the Belgian Federal Science Policy (contract SD/CS/01).

Supporting Online Material

www.sciencemag.org/cgi/content/full/329/5988/200/DC1
Materials and Methods
Figs. S1 to S6
Tables S1 to S5
References

7 April 2010; accepted 1 June 2010
10.1126/science.1190612

Explaining the Structure of the Archean Mass-Independent Sulfur Isotope Record

Itay Halevy,* David T. Johnston, Daniel P. Schrag

Sulfur isotopes in ancient sediments provide a record of past environmental conditions. The long–time-scale variability and apparent asymmetry in the magnitude of minor sulfur isotope fractionation in Archean sediments remain unexplained. Using an integrated biogeochemical model of the Archean sulfur cycle, we find that the preservation of mass-independent sulfur is influenced by a variety of extra-atmospheric mechanisms, including biological activity and continental crust formation. Preservation of atmospherically produced mass-independent sulfur implies limited metabolic sulfur cycling before ~2500 million years ago; the asymmetry in the record indicates that bacterial sulfate reduction was geochemically unimportant at this time. Our results suggest that the large-scale structure of the record reflects variability in the oxidation state of volcanic sulfur volatiles.

Most natural processes fractionate sulfur in proportion to the mass difference between the isotopes (*1*). Ultraviolet (UV) photolysis of atmospheric SO_2, however, produces a mass-independent fractionation (MIF) that is delivered to the surface only if atmospheric O_2 levels are very low (*2*–*7*). The presence of MIF in sedimentary sulfides and sulfates older than 2450 million years (My) and its absence from later sediments has led to the accepted view that atmospheric O_2 levels crossed a threshold value near the Archean-Proterozoic boundary (*2*–*6*). Beyond simply recording MIF, the Archean sulfur isotope record appears to carry a discernable temporal structure: moderate [<4 per mil (‰)] early Archean $\Delta^{33}S$ (*2*) anomalies, followed by a mid-Archean minimum (<2‰) and a late Archean explosion in the magnitude of MIF (<12‰ in $\Delta^{33}S$). Previous studies attribute this variability to changes in the composition and oxidation state of the atmosphere and the associated evolution of photochemical pathways (*7*–*9*). In addition, an asymmetry in the record, with strongly positive but only weakly negative isotopic anomalies, remains without a quantitative explanation.

Here we explore the effect of a variety of extra-atmospheric processes on the characteristics and preservation of MIF. We present an integrated model of the full surface-sulfur cycle, accounting for the production and translation of atmospherically derived MIF through a marine reservoir and its preservation in the geologic record (*10*). We use recent measurements and theoretical calculations of $^{3x}SO_2$ (x = 2, 3, 4, 6) UV absorption cross sections to constrain atmospheric MIF production (*10*–*12*). By solving mass-balance equations for the steady-state reservoir sizes and isotopic compositions of four different oxidation states of sulfur [S^{6+} (sulfate), S^{4+} (sulfite, SO_2), S^0 (elemental sulfur), and S^{2-} (sulfide, H_2S)], we track MIF from production to lithification.

Rates of volcanic supply, photolytic destruction, gas-phase reactions, and net deposition to the surface govern the atmospheric lifetime of SO_2. Any process that destroys atmospheric SO_2 at the expense of photolysis reduces the production, by mass, of MIF [for example, atmospheric oxidation (Fig. 1A)], but as long as photolysis rates are non-negligible relative to the other atmospheric SO_2 sinks, MIF is produced (though not necessarily preserved). In addition to nonphotolytic atmospheric sinks, which attenuate MIF by decreasing production, homogenization reduces MIF by remixing anomalous compositions back toward the original SO_2 value. Whereas atmospheric oxidation to sulfate has been discussed in this context (*6*), microbial processes, which can perform a similar function, have not been rigorously investigated (Fig. 1B). Given a quantitatively important flux of MIF from SO_2 photolysis, cycling between the sulfur reservoirs (e.g., microbial activity) or transformation to one oxidation state (e.g., quantitative reduction to sulfide) must be minor, as not to erase the anomaly. An immediate implication is that low atmospheric O_2 is necessary but insufficient for preservation of MIF in the geologic record.

Our model results illustrate the sensitivity of MIF to a few key properties of the ocean-atmosphere system, as well as its relative insensitivity to several other properties. Atmospheric deposition of SO_2 leads to its speciation in seawater [$SO_2(aq) \rightleftharpoons HSO_3^- + H^+ \rightleftharpoons SO_3^{2-} + H^+$], where subsequent oxidation by Fe^{3+} (*13*–*15*) leaves other aqueous oxidation pathways less important (for instance, Fe^{2+}-catalyzed oxidation by aqueous O_2 or by atmospherically produced H_2O_2). This leaves vanishingly little marine S^{4+} (~10^{-3} μM) and only modest sulfate concentrations (~10^2 μM). Given these oxidation rates, the absolute magnitude of MIF is only moderately sensitive to the adopted rate of S^{4+} disproportionation (Fig. 1D) (*10*), although the symmetry of

Department of Earth and Planetary Sciences, Harvard University, Cambridge, MA 02138, USA.

*To whom correspondence should be addressed. E-mail: itay.halevy@gmail.com